



Indium-doped TiO₂ nanoparticles for photocatalytic CO₂ reduction with H₂O vapors to CH₄

Muhammad Tahir¹, NorAishah Saidina Amin^{*}

Chemical Reaction Engineering Group (CREG)/Low Carbon Energy Group, Faculty of Chemical Engineering, Universiti Teknologi Malaysia, 81310 UTM, Skudai, Johor Baharu, Johor, Malaysia



ARTICLE INFO

Article history:

Received 6 February 2014

Received in revised form 8 May 2014

Accepted 22 June 2014

Available online 28 June 2014

Keywords:

Indium doped TiO₂

Photocatalysis

CO₂ reduction

Hydrocarbon fuels

Kinetic study

ABSTRACT

Indium (In)-doped titanium dioxide (TiO₂) nanoparticles were synthesized using a controlled sol-gel method. The structures and properties of the catalysts were characterized by XRD, FE-SEM, TEM, XPS, BET, UV-vis and PL spectroscopy. Indium, present over the TiO₂ in metal state, inhibited crystal growth and produced anatase phase of mesoporous TiO₂ nanoparticles. Doping In in TiO₂ also increased the surface area and enlarged the band gap. The photocatalytic activities of In-doped TiO₂ nanoparticles were considerably improved for CO₂ reduction with H₂O vapors in a cell type photoreactor. CO was observed as the main product over TiO₂, but doping In in TiO₂ remarkably increased the CH₄ yield. CH₄ production rate over 10 wt.% In-doped TiO₂ was 7.9-fold higher than the bare TiO₂ at 100 °C and CO₂/H₂O ratio of 1.43. In addition, C_{1–3} higher hydrocarbons namely C₂H₄, C₂H₆, C₃H₆ and C₃H₈ were detected in the product mixture. The enhanced photoactivity in mesoporous In-doped TiO₂ nanoparticles can be attributed to interfacial transfer of photogenerated charges, which led to effective charge separation and inhibited recombination of photogenerated electron-hole (e[−]/h⁺) pairs. Langmuir–Hinshelwood model, developed to investigate reaction rate parameters, fitted well with the experimental data.

© 2014 Elsevier B.V. All rights reserved.

1. Introduction

Global warming, primarily due to carbon dioxide (CO₂) emission in the atmosphere during fossil fuel combustion has invigorated considerable environmental issues. Therefore, technologies pertaining to carbon management, which not only mitigate global temperature, but can also fulfill partial energy needs are in demand [1]. Artificial photosynthesis is of significance importance due to water splitting to hydrogen (H₂) or CO₂ reduction with H₂O to hydrocarbon fuels and value added chemicals such as carbon monoxide (CO), methane (CH₄), methanol (CH₃OH), formic acid (HCOOH) and formaldehyde (HCHO). Thus, artificial photosynthesis provides alternative and sustainable pathways to resolve global environmental issues apart from resolving energy crises [2]. In this perspective, Inoue and Fujishima et al. [3] pioneered photocatalytic CO₂ reduction with H₂O as a reducing agent. The products observed were HCOOH, HCHO, CH₃OH and CH₄ in presence of both oxide

and non-oxide photocatalysts. Since then, significant efforts have been taken to design and develop selective photocatalytic system for efficient CO₂ reduction to value added chemicals and hydrocarbon fuels, but low photocatalytic activities have hindered the development. Therefore, better and more efficient photocatalysts are inevitable to maximize CO₂ conversion and yield rates with improved selectivity [4–7].

Among various semiconductor materials, the focus has been on the widely researched titanium dioxide (TiO₂) as photocatalyst. It is well established that TiO₂ has several advantages including higher oxidative potential, relatively cheap, abundantly available, non-toxic, and chemically/thermally stable [8,9]. However, TiO₂ is photoactive only under UV light irradiations due to its wide band gap energy (3.20 eV for anatase). Moreover, lower CO₂ reduction efficiency and selectivity, attributed to immediate recombination of photogenerated charges (e[−]/h⁺), has been reported over TiO₂. Therefore, it is imperative to modify TiO₂ structure to prevent recombination rate of electron and hole pairs for effective CO₂ photoreduction to value added chemicals and fuels [5].

Previously, different types of metals, non-metals and mesoporous materials have been investigated to improve TiO₂ photocatalytic activity. The addition of metals into TiO₂ structure could prevent recombination of electron-hole pairs. The more common researched metal-doped TiO₂ photocatalysts for CO₂

^{*} Corresponding author. Tel.: +60 7 553 5579; fax: +60 7 5588166.

E-mail addresses: noraishah@cheme.utm.my, profnoraishah@yahoo.com (N.S. Amin).

¹ Permanent address: Department of Chemical Engineering, COMSATS Institute of Information Technology Lahore, Punjab, Pakistan.

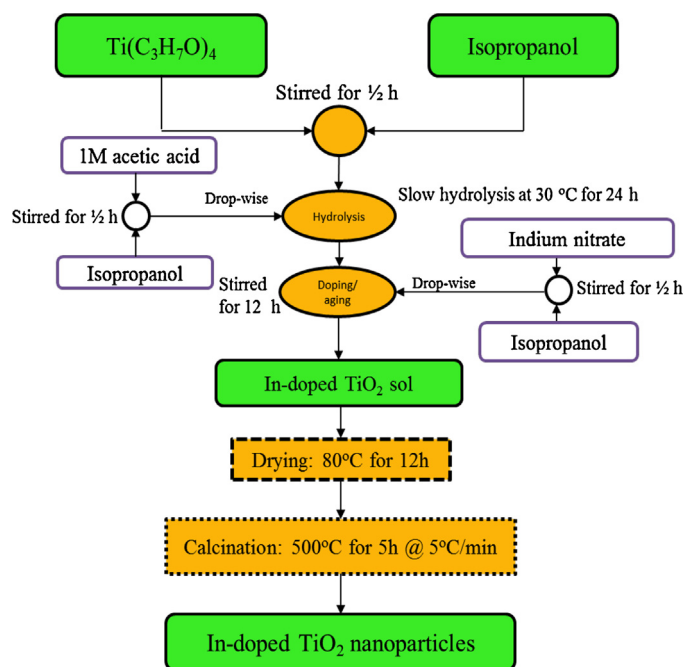


Fig. 1. Schematic of sol-gel method for preparation of In-doped TiO_2 nanoparticles.

reduction include Cu/TiO_2 [10–12], Rh/TiO_2 [13], N/TiO_2 [14], I/TiO_2 [15], $\text{N-Cu}/\text{TiO}_2$ [16], and Ag/TiO_2 [17]. Besides, In is considered as an efficient metal to enhance TiO_2 photoactivity and selectivity as In-metal has the ability to produce large number of electrons due to vacant d-orbits and can hinder photogenerated charges over TiO_2 .

The specific characteristics of In-metal include: (1) relatively cheaper, (2) multiple oxidation states (In^0 , In^{+1} , In^{+3}), (3) higher electron production, trapping and mobility, and (4) lower toxicity [18]. Poznyak et al. [19] investigated In_2O_3 modified TiO_2 for degradation of 2-chlorophenol and reported efficient separation of photogenerated charges in nanocrystalline $\text{In}_2\text{O}_3/\text{TiO}_2$ photocatalyst. Similarly, highly efficient N-doped In_2O_3 was observed during H_2 production through H_2O splitting [20]. In another study, H_2O splitting with higher H_2 yield rate was observed over $\text{In}_2\text{O}_3/\text{TiO}_2$ [21]. Recently, $\text{In}_2\text{O}_3/\text{C}_3\text{N}_4$ hybrid photocatalyst was investigated by Cao et al. [22] for CO_2 reduction to solar fuels. Higher CH_4 and H_2 yield rates were observed due to efficient production and separation of photogenerated electron-hole pairs (e^-/h^+), resulting in higher CO_2 reduction efficiency.

Due to the ability of In to produce large number of electrons with hindered recombination rate, it is appropriate to explore it further for CO_2 reduction applications. The objective of this study is to test the performance of In-doped TiO_2 nanoparticles for CO_2 photoreduction with H_2O vapors to hydrocarbon fuels using cell type photoreactor. The catalyst samples were characterized using XRD, FE-SEM, TEM, BET, XPS, UV-vis and PL spectroscopy. The operating parameters investigated were In-doping, reaction temperature, $\text{CO}_2/\text{H}_2\text{O}$ feed ratio and irradiation time for maximum yield rates. Langmuir-Hinshelwood model was developed to obtain fundamental insights for plausible reaction mechanism.

2. Experimental

2.1. Synthesis of indium doped TiO_2 nanocatalysts

Fig. 1 describes the schematic procedure for synthesis of In-doped TiO_2 nanoparticles. In-doped TiO_2 nanoparticles were prepared using a controlled sol-gel single step method using titanium (IV) iso-propoxide (Merck) and indium (III) nitrate (Merck).

The precursory of titanium solution was prepared with molar ratios: $\text{Ti}(\text{C}_4\text{H}_9\text{O})_4:15\text{C}_2\text{H}_5\text{OH}:2\text{CH}_3\text{COOH}$ (1 M). Typically, 10 mL of titanium tetra iso-propoxide was mixed in 30 mL of isopropanol and was stirred for 30 min in a 250 mL round bottom flask (sample A). In parallel, 6.37 mL of 1 M acetic acid was dissolved in 10 mL of isopropanol by stirring for 30 min (sample B). Hydrolysis process was conducted by adding drop wise sample B into sample A and vigorously stirring the mixture for 24 h at 30 °C. Next, an appropriate amount of indium nitrate was dissolved in isopropanol under constant stirring for 30 min. Both indium and titanium solution were stirred for 12 h until clear sol was produced. The sol was dried in the oven at 80 °C for 12 h under airflow. The dried sol was grinded to fine powder. Finally, the samples were calcined in a muffle furnace at a rate of 5 °C min^{-1} up to 500 °C and held at this temperature for 5 h. The bare TiO_2 nanoparticles were also prepared using the same procedure.

2.2. Characterization

In order to determine the structure and crystallinity of the samples, powder X-ray diffraction (XRD) was performed on Bruker D8 advance diffractometer ($\text{Cu-K}\alpha$ radiation, $\lambda = 1.54060 \text{ \AA}$, operated at 40 kV and 40 mA). The scanning rate was 1.2° min^{-1} from 10° to 70°. Field emission scanning electron microscopy (FE-SEM) was performed using JEOL JSM-6701F with EDX detector for calculating elements composition in photocatalysts. The particle size and lattice structure of the individual crystals were visualized by high-resolution transmission electron microscope (HR-TEM) with FEI-Tecni G2 Transmission Electron Microscope (TEM). Textural characterization of the samples was analyzed with a Micromeritics ASAP 2020. The N_2 adsorption-desorption properties were examined at 77 K. Specific surface area (S_{BET}) of monolayer coverage was determined using Brunauer-Emmett-Teller (BET) method. The pore size distribution was measured from the adsorption branch of the isotherm by means of Barrett-Joyner-Halenda (BJH) method. The XPS measurement was performed using Omicron DAR 400 analyser. The photocatalyst was fixed to the sample holder using carbon tape. The pass energy used was 20 eV, while the instrument was operated at 15 kV. The survey spectra were recorded in the range of 0–1400 eV. The binding energies were calibrated against the C1s signal (284.6 eV) as the internal standard. UV-vis absorption spectra of the samples were obtained from Shimadzu UV 3101 pc UV-Vis-NIR spectrophotometer. Finally, the recombination rate of the photogenerated electron-hole pairs (e^-/h^+) was estimated using Perkin Elmer LS 55 Luminescence spectrophotometer.

2.3. Photocatalytic activity test

The schematic presentation of the cell type photoreactor is illustrated in Fig. 2. The reactor consisted of a rectangular cell with 3 cm × 4 cm × 9 cm dimensions, and a total volume of 108 cm^3 . Photocatalytic activity was conducted over 0.25 g of powdered catalyst distributed uniformly at the bottom of the reactor chamber. A 10 mm thick quartz glass window covered the top of the reactor to enable effective transfer of irradiation from the 500 W mercury (Hg) flash lamp to the catalyst surface. The UV-light source, inserted inside the cold trap, have maximum irradiations intensity of 40 mW/cm^2 at wavelength 365 nm. The light intensity was measured with an optical process monitor, ILT OPM-1D, and XRD-340A sensor that was placed inside the reactor prior to the experiment. The lamp, connected to a high voltage power supply, was ignited through an igniter and a stabilizer. The reactor chamber and the lamp was covered with aluminum foil to ensure all the irradiations participating in the reaction came through the quartz window only.

The reactor, checked for leakage at 2 bar pressure for several hours, was purged using helium (He) carrier gas. Compressed CO_2

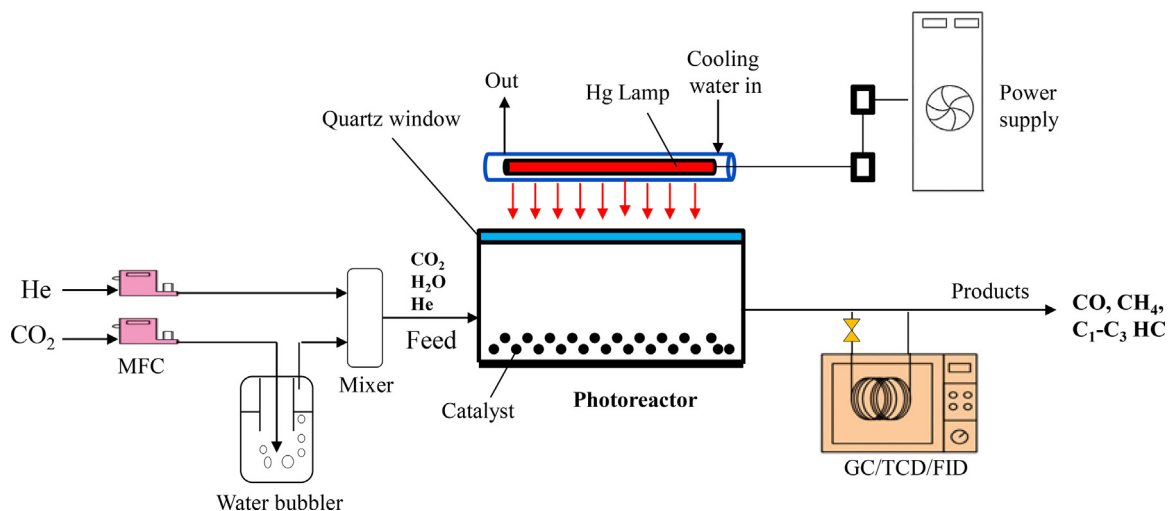


Fig. 2. Schematic of experiment setup for photocatalytic CO₂ reduction with H₂O vapors.

(99.99%) regulated by mass flow controller (MFC) was bubbled through water saturator to carry moisture. The CO₂ concentration was controlled using He (99.99%) as the diluent. The pressure inside the photoreactor was maintained at 0.20 bars above atmospheric pressure. The reactor was purged for one hour using a mixture of CO₂ and He prior to starting the experiment.

During photocatalysis process, the product mixture was analyzed using an on-line gas chromatograph (GC-Agilent Technologies 6890 N, USA) equipped with a thermal conductivity detector (TCD) and a flame-ionized detector (FID). Similarly, for offline analysis, gaseous products from the reactor were also taken using a gastight syringe (Agilent, 1000 μ L) having the same volume. The FID detector was connected with a HP-PLOT Q capillary column (Agilent, length 30 m ID 0.53 mm, film 40 μ m) for separation of C₁–C₆ paraffin and olefin hydrocarbons, alcohols and oxygenated compounds. The TCD detector was connected to UCW-982, DC-200, Porapak Q and Mol Sieve 13X columns. The UCW-982 was used for back flush and reversed flow to ensure C₆ and higher compounds could be detected earlier in the chromatogram. Meanwhile, C₁–C₂, C₃–C₅ compounds and light gasses (H₂, O₂, N₂ and CO) were separated using Porapak Q, DC-200, and MS-13X columns, respectively.

2.4. Calculation of yield rate and selectivity

The yield rate and selectivity of carbon containing products are calculated using Eqs. (1) and (2).

$$\text{Yield rate of } C_i (\text{mole g}^{-1} \text{ h}^{-1}) = \frac{\text{mole of } C_i \text{ in product}}{(\text{wt. of catalyst} \times \text{time})} \quad (1)$$

$$\text{Selectivity of product } C_i (\%) = \frac{C_i \text{ moles in product}}{\text{Total moles of C produced}} \times 100 \quad (2)$$

where C_i is the mole of carbon species (CO, CH₄, C₂H₄, C₂H₆, C₃H₆ and C₃H₈) in the product mixture and C is the moles of total carbon compounds produced.

3. Results and discussion

3.1. Structure and morphology of In-doped TiO₂

The XRD spectra of TiO₂ and In-doped TiO₂ samples are shown in Fig. 3. XRD peaks of the bare TiO₂ revealed pure crystalline and anatase phase calcined at 500 °C for 5 h. Similarly, all the peaks of the In-doped TiO₂ samples confirming the formation of anatase and

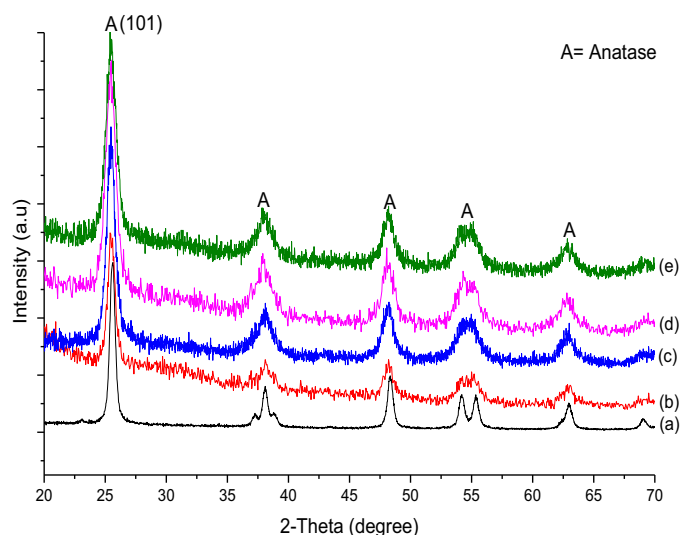


Fig. 3. XRD patterns of anatase TiO₂ and In-doped TiO₂ catalysts; (a) TiO₂, (b) 5 wt.% In/TiO₂, (c) 10 wt.% In/TiO₂, (d) 15 wt.% In/TiO₂ and (e) 20 wt.% In/TiO₂.

crystalline TiO₂ nanoparticles. However, all the peaks attributable to In in metal or oxide phase were not observed, even for the sample with 20 wt.% In-content. Furthermore, the TiO₂ anatase peaks become wider, while the intensities also increased with In doping, but no shifting in the TiO₂ peaks was observed. The wider anatase In-doped TiO₂ peaks indicate reduced TiO₂ crystallite size in presence of In. Furthermore, the ionic radius of In ion (0.081 nm) is larger than that of the lattice titanium ion (0.068 nm) [19]. Therefore, the possibility of In entering into the TiO₂ crystal cell was least. Thus, it is reasonable to deduce all the In was deposited over the TiO₂ surface as nanosized particles, which were not detectable by XRD. Similar observations have been reported in the literature for In-doped TiO₂ samples [20]. In order to confirm the crystallite shape of each sample, all the peaks were compared with the JCPDS-ICSD standards for anatase (89-4921). The diffraction peaks for TiO₂ appeared at 25.59°, 38.09°, 48.39°, 54.16°, 55.38°, 62.98° corresponded with (1 0 1), (0 0 4), (2 0 0), (1 0 5), (2 1 1) and (2 0 4) planes, confirming tetragonal anatase. Similarly, In-doped TiO₂ peaks are essentially equivalent with TiO₂, exhibiting peaks at 25.47°, 37.95°, 48.28°, 54.18°, 55.10°, and 62.98°, which are also consistent with (101), (004), (200), (105), (211) and (204) planes, matching to tetragonal anatase TiO₂.

Table 1
Cell parameters, crystallite sizes and EDX analysis of bare TiO₂ and In-doped TiO₂ samples.

Sample	Cell parameter (Å)		Cell volume (Å ³)	Crystallite size ^a (nm)	Surface elemental contents ^b (wt.%)		
	<i>a</i> = <i>b</i>	<i>c</i>			In	Ti	O
TiO ₂	3.764	9.486	134.39	19	0	67	33
5%In-TiO ₂	3.769	9.474	134.40	14	1.3	54.55	44.15
10% In-TiO ₂	3.773	9.462	134.66	11	2.4	53.30	44.40
15% In-TiO ₂	3.778	9.436	134.50	10	3.5	52.20	44.30
20% In-TiO ₂	3.773	9.455	134.65	9	4.6	51.30	44.10

^a Crystallite sizes calculated using Scherrer equation.

^b Surface elemental contents calculated using EDX.

The size of the crystallites in Table 1 was estimated using Scherrer equation based on XRD (1 0 1) peaks. At higher In content, smaller crystallites are obtained possibly due to In controlling TiO₂ crystal growth. The calculated crystallite sizes were 19, 14, 11, 10, and 9 nm for TiO₂, 5, 10, 15 and 20 wt.% In doped TiO₂ samples, respectively. Obviously, at higher In content, the decrease in crystallite size is significant. Similar observations have been reported in the literature [21]. Furthermore, cell parameters and cell volumes of TiO₂ and In-doped TiO₂ crystallites are summarized in Table 1. The cell parameters and cell volumes are comparable to those reported in JCPDS-ICSD (89-4921) standards for anatase TiO₂, i.e. *a* = *b* = 3.777 Å, *c* = 9.501, and *v* = 135.54 Å³. These observations confirmed fully developed tetragonal crystal shape of anatase TiO₂, while In-incorporation into TiO₂ lattice did not alter the cell structure.

Fig. 4 portrays the field emission scanning electron micrographs (FE-SEM) recorded in order to measure the morphology and particle

size of TiO₂ and In-doped TiO₂ nanoparticles. All the nanoparticles of TiO₂ are reasonably similar, thus minimizing the possibility of any unusual large particles as shown in Fig. 4(a). The uniform shape of the mesoporous spherical particles can be attributed to the TiO₂ crystal growth due to controlled hydrolysis process. Fig. 4(b) portrays micrograph of In-doped TiO₂ nanoparticles. The agglomeration is obvious, possibly due to the interaction of small crystallites. Similarly, particle size distribution and mesoporosity are presented in Fig. 4(c). The average In-doped TiO₂ particle size is in the range of 28–31 nm, which are larger compared to crystal size measured with XRD, reiterating possible agglomeration formations. EDX analysis also confirmed the presence of In-metal in In-doped TiO₂ sample as illustrated in Fig. 4(d). EDX spectra showed the appearance of peaks of O, In and Ti, indicating carbon was not detected in all the samples. The results of EDX elemental analysis of all the catalysts are presented in Table 1.

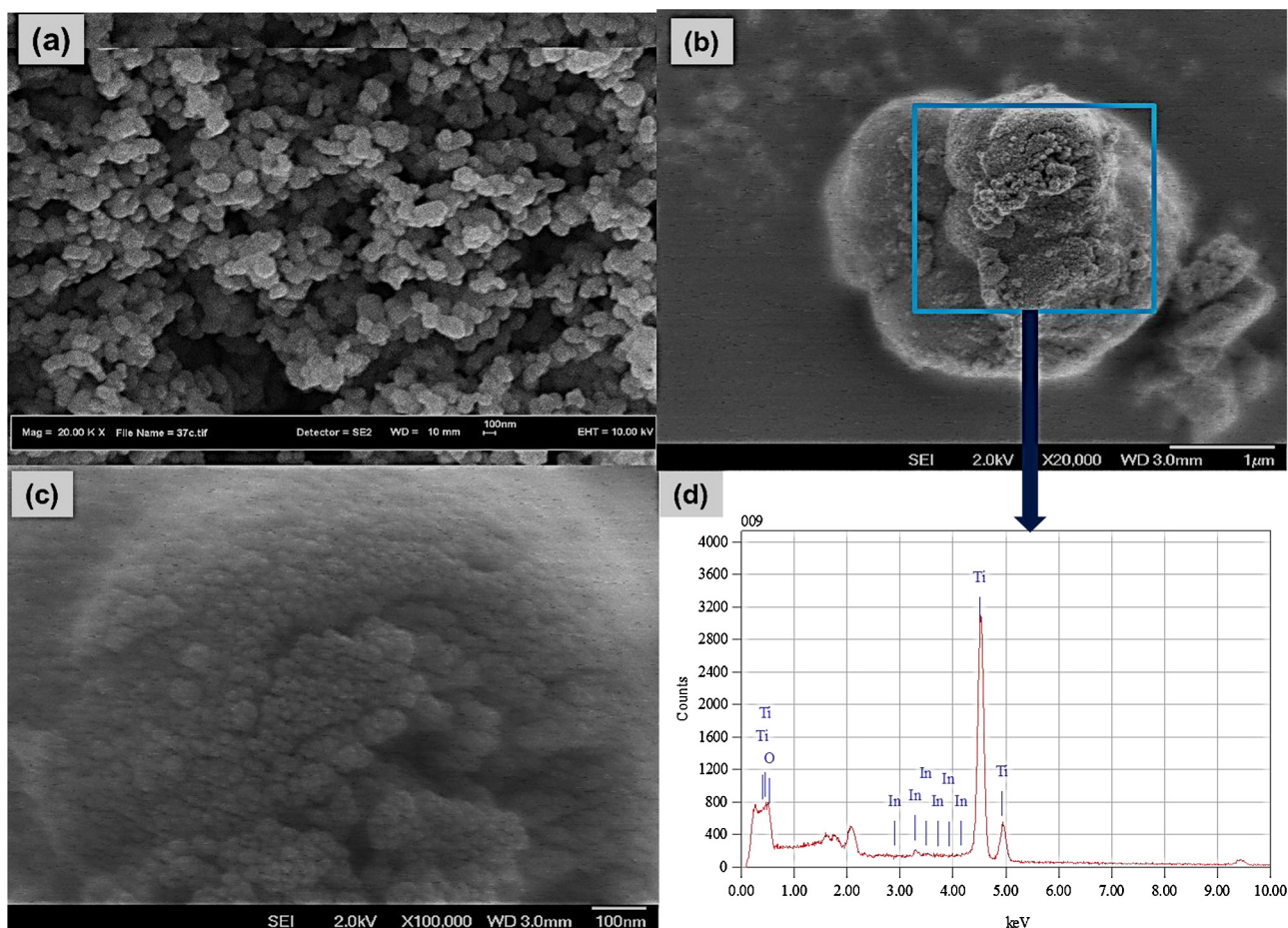


Fig. 4. FE-SEM micrographs of TiO₂ and 10 wt.% In-doped TiO₂ nanoparticles with EDX analysis: (a) TiO₂ nanoparticles, (b) FE-SEM image of In-doped TiO₂ at 1 μm, (c) FE-SEM image of In-doped TiO₂ at 100 nm, and (d) EDX spectrum of In-doped TiO₂ sample.

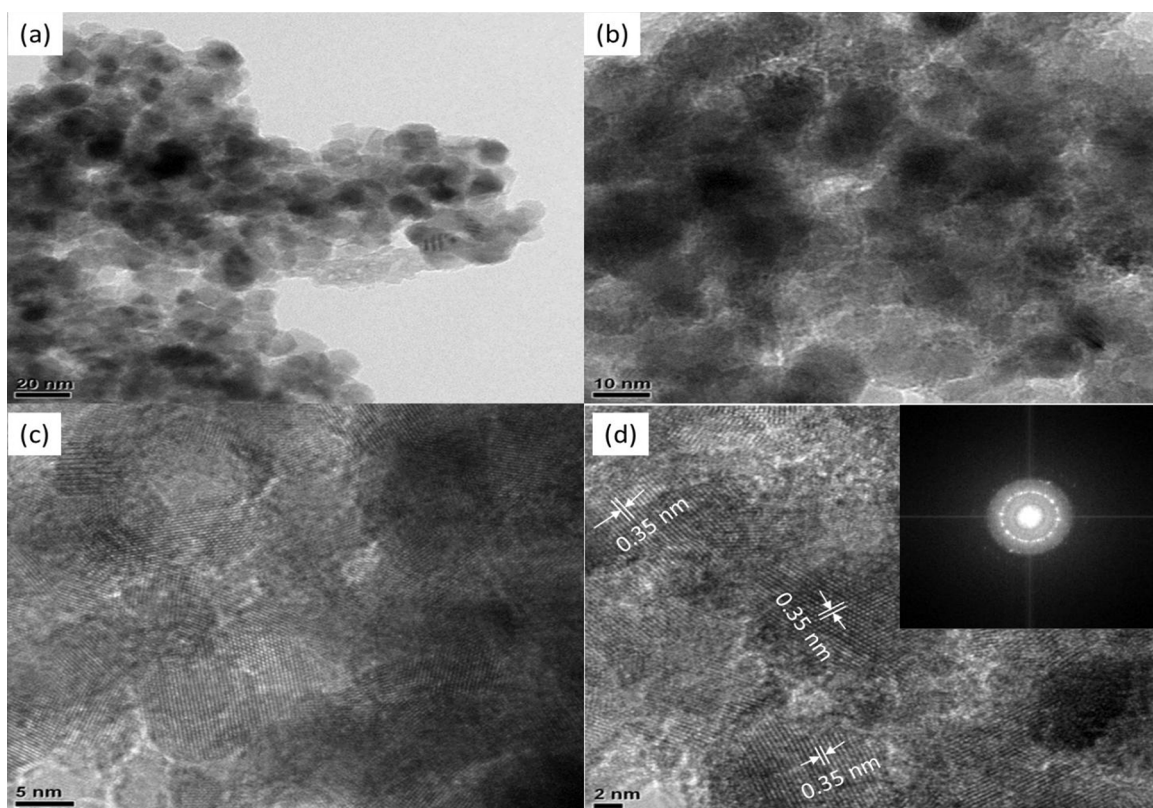


Fig. 5. TEM and HR-TEM images of 10 wt.% In-doped TiO₂ nanoparticles.

Fig. 5 exhibits the TEM micrographs of the In-doped TiO₂ nanoparticles. Mesoporous and uniform sized TiO₂ nanoparticles are obvious as depicted in Fig. 5(a and b), with the average particle size having diameter less than 13 nm, closer to the crystallite size estimated by Scherrer equation. The nanoparticles have inter-particle mesoporous structure, possibly due to the growth and aggregations of small particles. The HR-TEM images in Fig. 5(c and d) corroborated with the XRD morphology of TiO₂ nanoparticles, where 0.35 nm aligned anatase phase are grown along 101 directions. All the characterization results are in good agreement with previous reports [14,22].

3.2. Adsorption isotherms, surface area and pore structure analysis

Fig. 6 exhibits the N₂ adsorption–desorption isotherms of TiO₂ and In-doped TiO₂ nanoparticles. All the isotherms are similar to type IV curve of the hysteresis loops, conforming to mesoporous materials [23]. The mesoporous structure of TiO₂ and In-doped TiO₂ samples without surface directing agents was evidently due to the controlled hydrolysis process. Furthermore, the initial part of the isotherms (at low P/P_0) is related to the monolayer–multilayer adsorption on the internal surface. However, at higher P/P_0 , the steep increment in the adsorption volume is attributed to the capillary condensation as the pores were saturated with liquid. The monolayer–multilayer was more dominant in TiO₂ samples in which capillary action started at $P/P_0 = 0.60$. Both the capillary and condensation processes are prominent in In-doped TiO₂ samples at $P/P_0 = 0.55$.

The surface area, pore volume and pore size of all samples are summarized in Table 2. The BET surface area of TiO₂ was 42.98 m²/g, increased to 61, 84, 98 and 123 m²/g with 5, 10, 15 and 20 wt.% In doping respectively. The t -plot external surface area increased, while t -plot micropore surface area reduced significantly with In

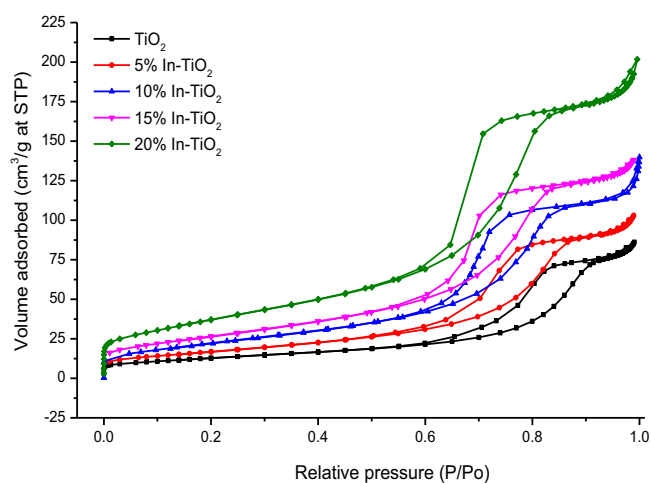


Fig. 6. N₂ adsorption–desorption isotherms of TiO₂ and In-doped TiO₂ samples.

doping. Larger surface area can also be attributed to the suppression of TiO₂ crystal growth by In. Furthermore, the mesoporous structure of TiO₂ and In-doped TiO₂ catalysts without the addition of surface directing agents is supposedly due to the controlled hydrolysis process using diluted acetic acid. Similarly, BJH adsorption pore volume increased while pore diameter decreased with In doping. Thus, the increase in pore volume with reduced pore diameter was possibly due to the controlled crystal growth in the In-doped TiO₂ samples. All these results are consistent with previous reports [24].

3.3. Chemical state of elements in In-doped TiO₂

The chemical state of Ti, In, O, and C in In-doped TiO₂ was determined by X-ray photoelectron spectroscopy (XPS). The Ti 2p

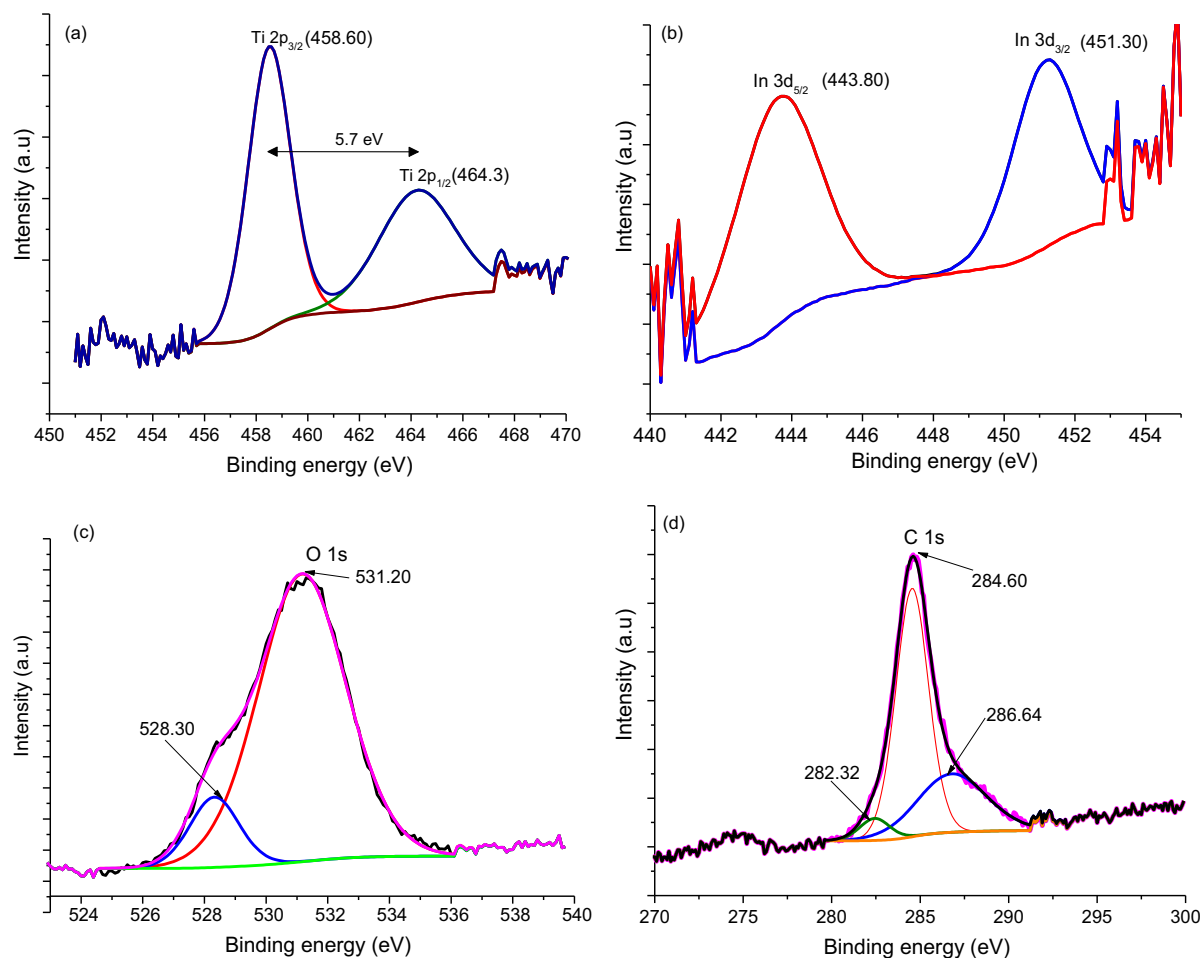
Table 2Summary of physiochemical characteristics of TiO₂ and In-doped TiO₂ samples.

Type of catalyst	Surface area (m ² /g)				Pore volume (cm ³ /g)		Pore width (nm)	Band gap (eV)
	BET surface area	t-Plot micropore area	t-Plot external surface area	BJH adsorption surface area	t-Plot micropore volume	BJH adsorption pore volume	BJH pore width	
TiO ₂	43	8.93	34	52	0.00387	0.13	10.33	3.12
5% In-TiO ₂	61	0.74	61	69	0.00046	0.16	9.34	2.19
10% In-TiO ₂	84	2.85	95	113	0.00073	0.22	7.67	3.20
15% In-TiO ₂	98	1.85	112	143	0.00023	0.28	7.50	3.22
20% In-TiO ₂	123	3.56	124	170	0.00184	0.32	7.38	3.24

spectrum in Fig. 7(a) shows the peaks with binding energies (BE) located at ~458.60 eV (2p_{3/2}) and 464.30 eV (2p_{1/2}), indicating titanium in Ti⁴⁺ oxidation state. Fig. 7(b) shows the In-3d spectrum peaks of In 3d_{5/2} and In 3d_{3/2} with BE region centered at ~443.80 and 451.30 eV, respectively, characteristics of In in metal state. The spectrum of O 1s shown in Fig. 7(c), reveal two peaks centered at 528.30 and 531.20 eV. The BE value of 528.30 eV is assigned to the lattice oxygen O²⁻ bound to anatase Ti and is in agreement with the reported values [16]. The oxygen peak at around 531.20 eV are possibly due to the free hydroxyl group (OH⁻). The C 1s spectrum of all the carbon peaks is shown in Fig. 7(d). The peak with binding energy located at ~284.60 eV is assigned to elemental carbon (C–C) while, the one at 586.64 eV corresponds to C–O. The other peak at 282.30 eV is possibly due to substitution of oxygen by carbon in TiO₂. The presence of carbon may be recognized as the carbon from carbon tap used for analysis of sample, since in EDX carbon containing compound was not observed.

3.4. UV-vis and photoluminescence spectroscopy

The UV-vis absorbance spectra of TiO₂ and In-doped TiO₂ samples are depicted in Fig. 8. The absorption band edge of TiO₂ was located at 398 nm, which indicates an obvious red shift in the wavelength of TiO₂ compared to the standard anatase TiO₂ ($\lambda \sim 380$ nm) catalyst. However, the TiO₂ absorption edge slightly shifted toward the longer wavelengths by incorporating In into the TiO₂ structure. The band gap energy (eV) of the samples was calculated using Tauc equation. The E_{bg} values of all the samples were measured from a plot of $(\alpha h\nu)^2$ versus $(h\nu)$ using direct method as shown in Fig. 9. The E_{bg} estimated from the intercept of the tangents to the plots is 3.12 eV for TiO₂, but shifted to higher values with In doping as tabulated in Table 2. The increase in the band gap energy was probably due to the higher In₂O₃ band gap energy ($E_{bg} = 3.7$ eV) [25,26]. The shift in TiO₂ band gap energy toward ultraviolet regions has been reported in literatures for In-doped TiO₂ nanoparticles

**Fig. 7.** XPS spectra of 10 wt.% In-doped TiO₂ sample: (a) spectra of Ti 2p, (b) In 3d, (c) O 1s, and (d) C 1s.

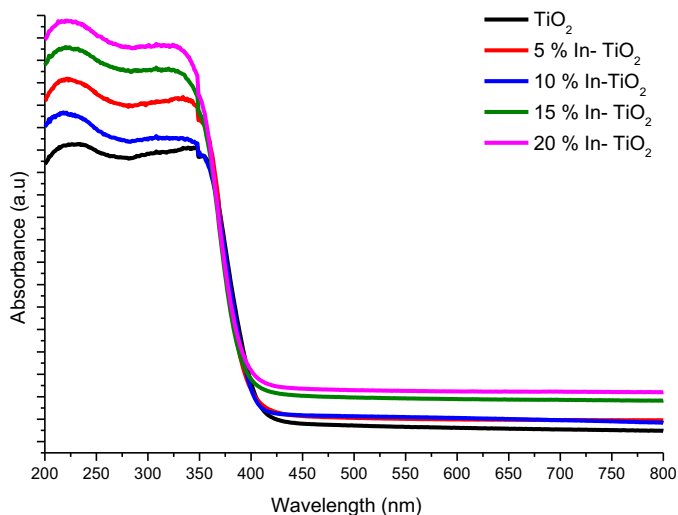


Fig. 8. UV-vis absorption spectra of TiO₂ and In-doped TiO₂ catalysts.

[21,27]. Therefore, incorporation of In in the crystalline and mesoporous TiO₂ allows the formation of a UV semiconductor, which could also inhibited the recombination of photogenerated charges.

Fig. 10 compares the photoluminescence (PL) spectra for TiO₂ nanoparticles and In-doped TiO₂ samples with different In content. In doped TiO₂ nanoparticles exhibited PL signal with similar curve shape, demonstrating In presence did not result into a new PL phenomenon. In-doped TiO₂ nanoparticles exhibited a wide and strong PL signals in the range of 450–550 nm with the excited wavelength of 350 nm. The spectral peak located at 458 nm corresponds to anatase TiO₂ while two peaks at 483 and 527 nm are attributed to the transition from the oxygen vacancies with two and one trapped electron to the TiO₂ valance band, respectively. Due to oxygen vacancies, the photogenerated electrons in the conduction band initially reached the vacant space and then recombined with the photogenerated holes in the valance band to produce fluorescence emission [19,20]. However, TiO₂ band is more intense while the In-doped TiO₂ band intensities gradually weakened. The reduced PL intensity for In-doped TiO₂ catalysts is possibly due to the In incorporated into TiO₂, hindering electron–hole pairs recombination rate on the In-doped TiO₂ surface. In other words, the recombination of photogenerated carriers via transition from the

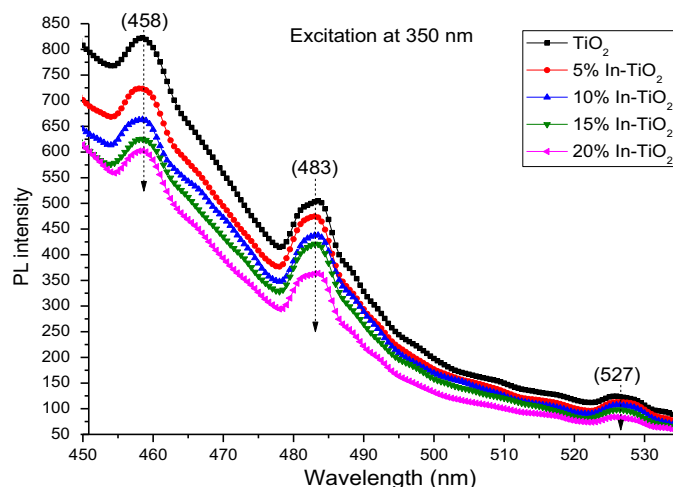


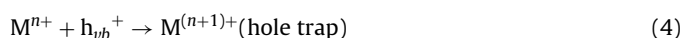
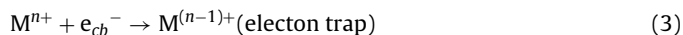
Fig. 10. PL emission spectra of TiO₂ and In-doped TiO₂ catalysts.

oxygen vacancies to TiO₂ valance band was suppressed efficiently upon doping with In-ions [20,21].

3.5. Photocatalytic activity of CO₂ with H₂O

Prior to CO₂ photoreduction activity test, a series of preliminary tests were conducted in the absence of CO₂ and H₂O under UV light irradiations for a period of 2 h at 100 °C for the following cases; (1) empty reactor and He, (2) reactor with TiO₂ nanoparticles and He and (3) reactor with In-doped TiO₂ photocatalysts and He. In all cases, reaction products were not detected, confirming no organic residues photodecomposition in the catalyst, if any. Additional preliminary tests were conducted using H₂O vapors and He in presence of photocatalyst under UV irradiations. Again, in either case no carbon-containing compounds were observed. These results confirmed photoreduction products were obtained from CO₂ source only. Therefore, it is reiterated that the photocatalytic reduction processes require all three components, i.e. catalyst, feed (CO₂, H₂O), light source and any carbon containing compounds should be produced from CO₂ through photocatalytic reactions. All the photocatalytic CO₂ reduction experiments were repeated at least in triples and aggregated results are reported.

The effects of In-doping into TiO₂ for photocatalytic CO₂ reduction with H₂O vapors are exhibited in Fig. 11. The doping of In-ions over TiO₂ surface led to higher photoactivity for CO₂ photoreduction. CH₄ yield was low over pure TiO₂, but gradually increased up to 10 wt.% In-content, before decreasing with more In-contents. The maximum CH₄ yield produced was 1156 μmole g-catal.^{−1} over 10 wt.% In-doped TiO₂ catalyst compared to 73 μmole g-catal.^{−1} using bare-TiO₂ when irradiated for 2 h. Thus, the optimum amount of In-content doped into TiO₂ was 10 wt.%, revealing effect of In was more extensive. The significant increments in CH₄ yield over In-doped TiO₂ was possibly due to the ability of In to trap electrons and/or holes and alter their recombination rates through the processes explained in Eqs. (3) and (4).



Therefore, In-doping can promote the charge pair separation of TiO₂ photocatalyst for higher CO₂ reduction efficiency. Photoexcited electrons in the TiO₂ conduction band can be accepted and transferred efficiently to CO₂, functioning as an efficient reducing agent. The electrons can also be scavenged by O₂ which in turn produces superoxide O₂[−]. The positive holes in the valance band can be trapped by OH[−] or H₂O species adsorbed over TiO₂

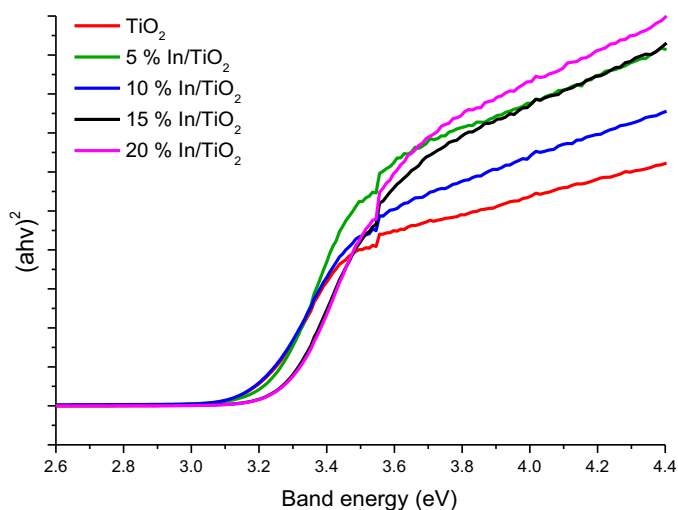


Fig. 9. Band gap energy calculations from absorption spectra of TiO₂ and In-doped TiO₂ catalysts.

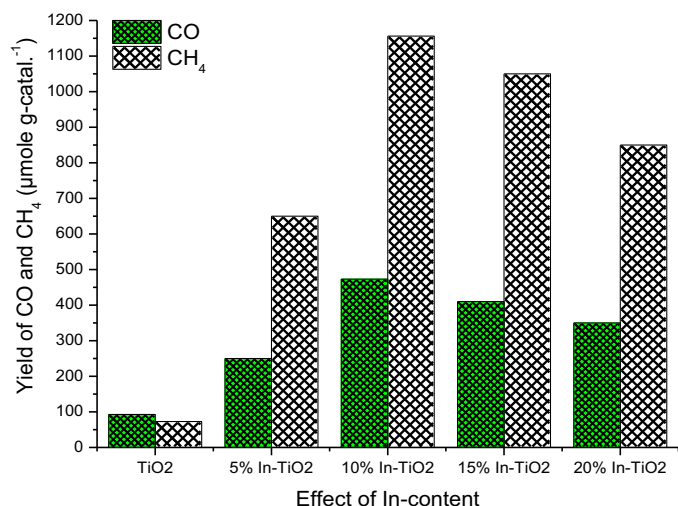


Fig. 11. Effect of In-contents on TiO₂ activity for the production of CO and CH₄ (irradiation time = 2 h, T = 100 °C, P_{H₂O} = 0.042 bars and P_{CO₂} = 0.02 bars).

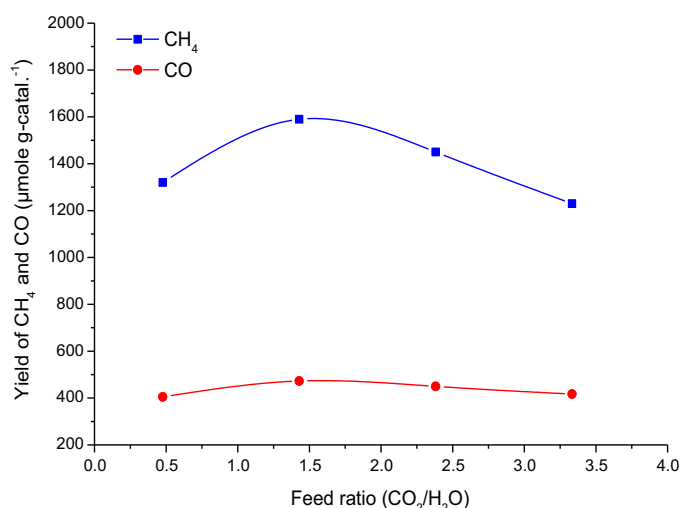


Fig. 12. Yield of CO and CH₄ at various initial CO₂/H₂O feed ratios over 10 wt.% In-doped TiO₂ (irradiation time 4 h, reaction temperature 100 °C).

surface. These processes promote the separation of photogenerated electron-hole pairs (e^-/h^+) to accelerate CO₂ reduction process, enhancing In-doped TiO₂ catalytic performance. In general, doping In into TiO₂ helps to trap photogenerated electrons and hindered photogenerated charges recombination, which is one of the limiting factors in TiO₂ photoactivity [28,29]. However, excess In-content reduced TiO₂ photoactivity, possibly due to establishing charge recombination centers inside the TiO₂ structure. Furthermore, excess In-dispersion over the TiO₂ surface probably masked its surface resulting in less light exposure for production of electron-hole pairs [30]. Higher concentration of In-ions leads to the recombination of photogenerated electrons and holes according to Eqs. (5) and (6):



Fig. 12 depicts the relationship between CH₄ and CO yields and feed ratio of CO₂/H₂O in the initial feed stream. The yield of CH₄ increased with relatively larger concentration of CO₂ adsorbed over the In-doped TiO₂ surface at higher CO₂/H₂O feed ratios. However, after CO₂/H₂O feed ratio of 1.43, a significant reduction in the CH₄

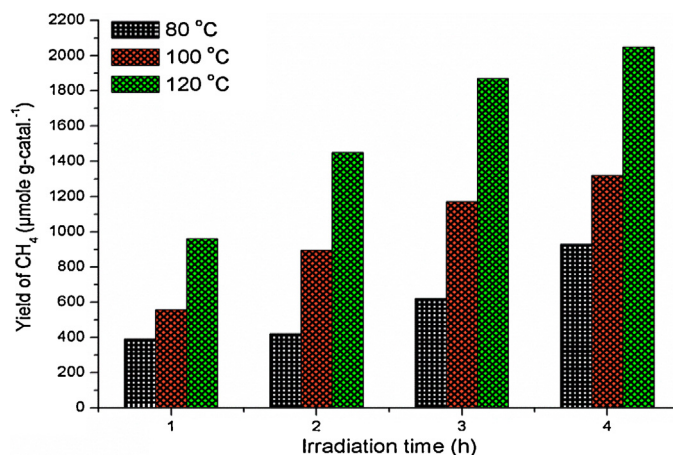


Fig. 13. Effect of reaction temperature on the yield of CH₄ production over 10 wt.% In-doped TiO₂ catalyst at CO₂/H₂O feed ratio 1.43.

yield was observed, possibly due to lower concentration of H₂O molecules adsorbed at the catalyst surface to react with CO₂. Similarly, the decrease in the yield of CO at higher CO₂/H₂O feed ratio was observed. This phenomenon implied a competitive adsorption of both the reactants, i.e. CO₂ and H₂O vapors on the active sites of the photocatalyst. At lower feed ratios (lower CO₂ concentration), H₂O molecules would cover most of the catalyst surface, thus CO₂ would compete with H₂O molecules. Conversely, at much higher feed ratio (higher CO₂ concentration), reaction rate was reduced possibly due to H₂O molecules having to compete with adsorbed CO₂ to react. Therefore, an optimum concentration of CO₂ and H₂O feed ratios could enhance CO₂ photoreduction process to obtain maximum yield rates [23,31].

The amount of CH₄ produced during photocatalytic CO₂ reduction over 10 wt.% In-doped TiO₂ at different reaction temperatures (80, 100 and 120 °C) is presented in Fig. 13. Obviously, a significant increase in CH₄ yield could be seen at higher temperature, demonstrating higher CO₂ photoreduction rate. The enhanced CO₂ photoreduction process at elevated temperature could be explained on the basis of efficient reactant adsorption and product desorption over the catalyst surface. At higher temperature, more photoactive sites of catalysts are available to capture CO₂, possibly due to efficient desorption of products. Therefore, higher temperature gave positive effects on photocatalytic reactions particularly in gas phase reactions and can accelerate the reaction rate. Higher temperature also reduces activation energy as similarly observed previously [32,33].

Fig. 14 demonstrates the effect of reaction time on the yield of CO and CH₄ over TiO₂ and In-doped TiO₂ catalysts. CO and CH₄ concentrations gradually reached to steady state in the entire irradiation period. Over TiO₂, CO was observed as the main product, while the yield of CH₄ was enhanced significantly over the In-doped TiO₂ catalyst, possibly due to efficient production and trapping of electrons by In. This can also be explained based on the semiconductor conductance band potentials. The conductance band (CB) of TiO₂ is 0.50 eV at pH 7 while the reduction potential of CO₂/CH₄ is -0.24 eV. Since the conductance band potential is more negative than CO₂/CH₄ reduction potential, the reaction is theoretically feasible. In addition, CH₄ needs 8 electrons compared to 2 electrons for CO production. Higher CH₄ production over the In-doped TiO₂ was probably due to a more negative conductance band and higher production of electrons being trapped by In-metal. Similar observations have been reported in the literatures for the photocatalytic CO₂ reduction with H₂O over montmorillonite modified TiO₂ catalysts [23,34].

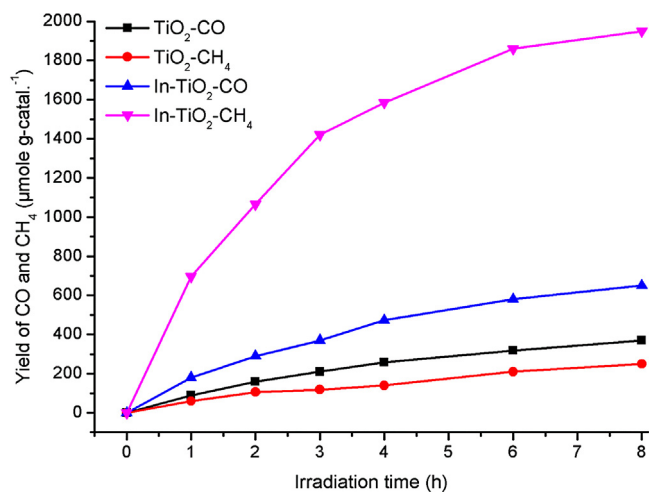


Fig. 14. Effect of irradiation time on CO₂ reduction to CO and CH₄ using TiO₂ and 10 wt.% In-doped TiO₂ catalyst (reaction temperature 100 °C, CO₂/H₂O feed ratio 1.43).

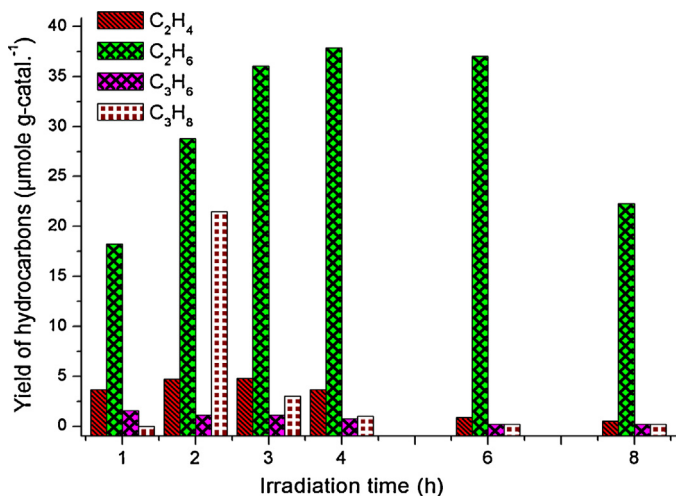


Fig. 15. Effect of irradiation time on photocatalytic CO₂ reduction to hydrocarbons over 10 wt.% In-doped TiO₂ catalyst (reaction temperature 100 °C, CO₂/H₂O feed ratio 1.43).

Fig. 15 exhibits the amount of C₂H₄, C₂H₆, C₃H₆ and C₃H₈ hydrocarbons in the product mixture produced during CO₂ reduction with H₂O over the 10 wt.% In-doped TiO₂ catalyst. Initially, the hydrocarbons yield increased markedly, but then gradually reduced with prolonged time attributable to hydrocarbons undergoing photoreduction with CO₂ or reverse oxidation reactions. Among the hydrocarbons, C₂H₆ yield was appreciable over the entire irradiation time confirming In-doped TiO₂ catalyst was suitable for production of higher hydrocarbons especially ethane. This could also be explained based on reaction mechanism as intermediate species $\cdot\text{CH}_3 - \cdot\text{CH}_3$ could combine to produce C₂H₆ instead of CH₄. The yields of all the products were in the order of CH₄ > CO > C₂H₆ > C₂H₄. The yield rates of all products are summarized in Table 3. The operating parameters employed during photocatalytic CO₂ reduction with H₂O vapors in cell type photoreactor are presented in Table 4. The yield rate of CH₄ over In-doped TiO₂ catalysts is 244 μmole g-catal.^{−1} h^{−1}, 7.9-fold higher than CH₄ yield rate over bare TiO₂. In addition, CO yield rate over the In-doped TiO₂ is 81 μmole g-catal.^{−1} h^{−1}, 2 times higher than CO yield rate over TiO₂. Therefore, In-doped TiO₂ catalyst is efficient for the production of CH₄ and CO. The observed selectivity was 69% and 29%, for CH₄ and CO, respectively. An appreciable amount of C₂–C₃

Table 3

Summary of product yield rates during photocatalytic CO₂ reduction using different catalysts.

Products	Yield rates (μmole g-catal. ^{−1} h ^{−1}) ^a		Selectivity (%)	
	TiO ₂	10 wt.% In/TiO ₂	TiO ₂	10 wt.% In/TiO ₂
CH ₄	31	244	40	69.29
CO	46	81	60	29.66
C ₂ H ₄	0.00	0.06	0.0	0.022
C ₂ H ₆	0.00	2.78	0.0	1.020
C ₃ H ₆	0.00	0.02	0.0	0.007
C ₃ H ₈	0.00	0.02	0.0	0.007

^a Yield rates calculated at 8 h irradiation basis, $P_{\text{CO}_2}/P_{\text{H}_2\text{O}} = 1.43$ bars.

Table 4

Summary of operating parameters employed in cell type reactor.

System	TiO ₂	10 wt.% In/TiO ₂
Volume	106 cm ³	106 cm ³
Catalyst loading	0.25 g TiO ₂	0.25 g In/TiO ₂
Light source	500 W Hg, λ = 365 nm, I = 40 mW/cm ²	500 W Hg, λ = 365 nm, I = 40 mW/cm ²
Temperature	373 K	373 K
Pressure	0.20 bar	0.20 bar
Main product	CH ₄ , CO	CH ₄ , CO
Yield rate (CH ₄ /CO) ^a (μmole g-catal. ^{−1} h ^{−1})	31/46	244/81

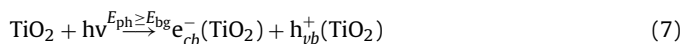
^a Yield rates calculated at 8 h irradiation basis, $P_{\text{CO}_2}/P_{\text{H}_2\text{O}} = 1.43$ bars.

hydrocarbons namely C₂H₄, C₂H₆, C₃H₆ and C₃H₈ are produced over In-doped TiO₂ catalyst. Significantly higher CH₄ production rate with appreciable amounts of hydrocarbons reveals efficient production of electrons and their utilizations during photocatalytic CO₂ reduction process over mesoporous In-doped TiO₂ nanoparticles.

3.6. Mechanism of CO₂ photoreduction with H₂O

In photocatalysis process, when photons having energy equal or higher than the band gap energy are adsorbed by the semiconductor, then electrons (e_{cb}^-) and holes (h_{vb}^+) are produced. Due to their short life time, they can recombine in bulk or on the surface within nanoseconds or can be trapped on surface state, where they react with acceptor or donors. During photocatalytic CO₂ reduction with H₂O vapors over TiO₂ catalyst under UV light irradiations, electrons (e^-) are transferred from the TiO₂ conduction band for the photoreduction of CO₂, yielding $\cdot\text{CO}_2^-$ radicals. On the other hand, holes (h^+) are transferred to H₂O initiating its photooxidation, yielding hydrogen ions (H⁺) and hydroxyl radical ($\cdot\text{OH}$). The hydroxyl radicals further oxidized with H₂O for the production of O₂ and H⁺ [35]. The $\cdot\text{H}$ radicals originated during reduction of proton reacted with carbon radicals on the catalyst surface to produce intermediates $\cdot\text{CH}_2$ and $\cdot\text{CH}_3$ radicals and finally CH₄ and higher hydrocarbons. All possible reaction steps during photocatalytic CO₂ reduction with H₂O are explained by Eqs. (7)–(24) [18,36,37].

Generation and separation of charges over Indoped TiO₂



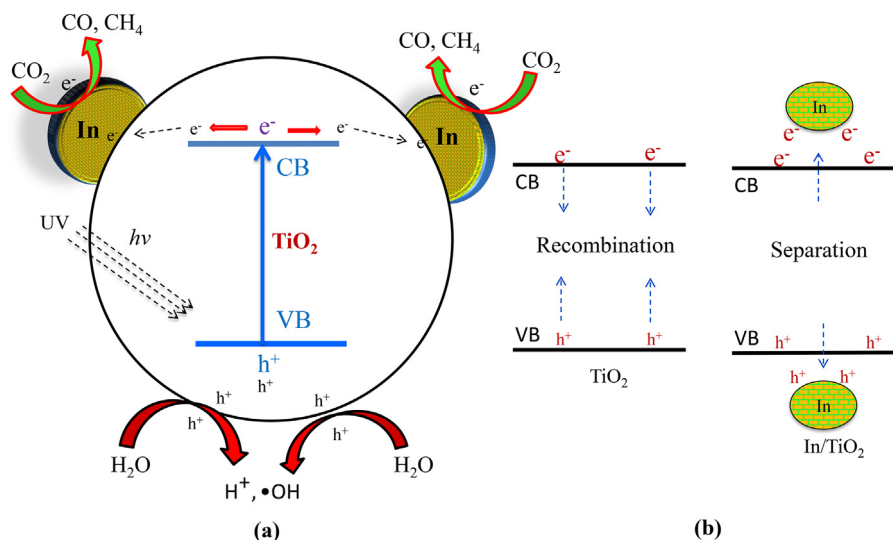
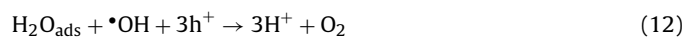
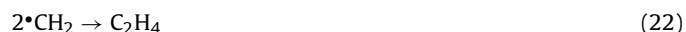


Fig. 16. Schematic of plausible reaction mechanism for photocatalytic reduction of CO₂ with H₂O: photocatalytic CO₂ reduction process: (a) oxidation and reduction process over In-doped TiO₂, and (b) recombination and separation of charges.

Oxidation and reduction process



Mechanism of hydrocarbon production



During TiO₂ photocatalysis, large number of electrons and holes are produced over mesoporous and anatase TiO₂ nanoparticles, shifting TiO₂ in highly excited state Ti³⁺–O[•] as explained in Eq. (7) and (8). The photogenerated electron could trap to produce unproductive heat as illustrated in Eq. (9). However, the excited electrons can be efficiently transferred over nanosized TiO₂, possibly trapped by In-metal if any, thus resulting in efficient transfer of electrons and holes for oxidation and reduction processes as explained in Eq. (10). The photogenerated electron undergoes CO₂ reduction to produce excited CO₂ molecules, while holes react with adsorbed H₂O molecules to precede oxidation process, as illustrated in Eqs. (11)–(14). The intermediate photogenerated species undergoes through different reactions, thus producing CO, CH₄ and hydrocarbons, as explained in Eqs. (15)–(24).

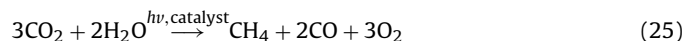
Since all of the above products were detected experimentally, CH₄ was confirmed to be produced from methyl radicals (•CH₃). These radicals were directly dependent on the formation of the intermediate product, CO. The production of higher CH₄ yield rate

and other higher hydrocarbons also confirmed efficient H₂O oxidation and CO₂ reduction process over In-doped TiO₂ catalysts, obviously due to significant production of electron–holes being trapped by In-metal. Similar observations were reported by Saladin et al. [32] during gas phase reduction of CO₂ with H₂O over TiO₂ surface. From the reaction summary and in view of the above observations, there is ample probability to produce hydrocarbons using metal-doped TiO₂ having good reduction potentials. However, further investigations are required to postulate feasible reaction mechanisms and predict possible reaction products.

The schematic presentation of photocatalytic CO₂ reduction with H₂O over 10 wt.% In-doped TiO₂ catalyst is presented in Fig. 16(a and b). Under light irradiations, there was efficient production and absorption of electrons over both catalysts. Subsequently, electrons were transferred from TiO₂ conduction band to In-metal, trapped by CO₂ molecules, leading to CO₂ reduction process. A series of reactions take place over 10 wt.% In-doped TiO₂ for possible higher yield rates of C₁ to C₃ paraffins and olefins.

3.7. Langmuir–Hinshelwood model

In heterogeneous catalysis, surface reaction rates are supposed to depend on the fraction of active sites covered by different species. For an irreversible bimolecular reaction between the molecules that are competitively adsorbed on the same type of active sites, the reaction rate depends on the probability that molecules are on the adjacent sites. Furthermore, this probability may also be proportional to the product fractional coverage. The bimolecular photocatalytic reaction for CO₂ reduction can be explained using Eq. (25).



The surface reactions are usually assumed to be the slowest step and eventually the rate controlling step. If the reactants are competitively adsorbed on the same adsorption sites with different rate constants, then such reactions can be postulated by a Langmuir–Hinshelwood (L–H) mechanism. For photocatalytic type reactions, when CO₂ and H₂O were assumed to be adsorbed on the same active sites on the catalyst surface, the rate of Eq. (25) could be obtained using L–H model as described in Eq. (26).

$$\text{Rate} = (kI^{\alpha}) \left(\frac{K_{\text{H}_2\text{O}}P_{\text{H}_2\text{O}}K_{\text{CO}_2}P_{\text{CO}_2}}{(1 + K_{\text{H}_2\text{O}}P_{\text{H}_2\text{O}} + K_{\text{CO}_2}P_{\text{CO}_2} + K_{\text{CO}}P_{\text{CO}} + K_{\text{O}_2}P_{\text{O}_2} + K_{\text{CH}_4}P_{\text{CH}_4})^2} \right) \quad (26)$$

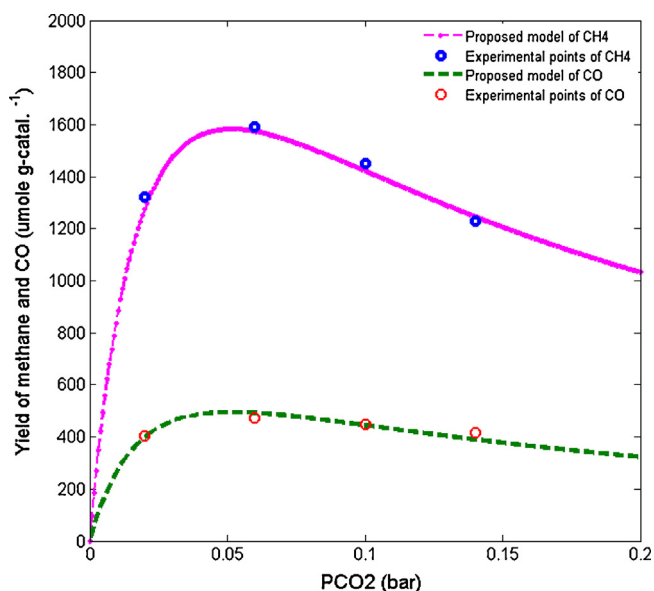


Fig. 17. Profile of Langmuir–Hinshelwood model for photocatalytic CO₂ reduction over 10 wt.% In-doped TiO₂ catalyst.

where k is the rate constant of any particular product, I is UV flux intensity in which kinetic constants are evaluated. In general, the photocatalytic reaction rate is proportional to I^α , where α is the reaction order of light intensity, having value one or less, depending on the light intensity. K_{H_2O} , K_{CO_2} , K_{CO/KO_2} and K_{CH_4} are the ratios of rate constants for adsorption and desorption of H₂O, CO₂, CO, O₂ and CH₄, respectively. Eq. (26) can be simplified assuming only reactants are adsorbed on the catalyst surface, while all the products are desorbed immediately after chemical reaction. Thus, CO₂ and H₂O were adsorbed on the surface of the catalyst and the modified form of L–H model becomes Eq. (27).

$$\text{Rate of reaction} = (kI^\alpha K_{H_2O} K_{CO_2}) \left(\frac{P_{H_2O} P_{CO_2}}{(1 + K_{H_2O} P_{H_2O} + K_{CO_2} P_{CO_2})^2} \right) \quad (27)$$

The constants of the L–H model were determined by correlating with the experimental data. As shown in Fig. 17, the model and the experimental data fitted well confirming adsorption of CO₂ and H₂O over the catalyst surface were without dissociations. It has been observed that the reaction rate is proportional to P_{CO_2} at a lower partial pressure, when only a small fraction of the sites are occupied. However, as P_{CO_2} increases, the rate becomes less dependent on it, gradually slows down possibly due to adsorption of CO₂ over the entire catalyst surface. Under such circumstances, H₂O molecules have to compete with CO₂ molecules for chemical reactions, resulting in lower rate of reaction. The light intensity used to simulate the L–H model, Eq. (27) is 40 mW/cm², while intensity factor (α) value obtained is 0.75. The CO₂ adsorption constant K_{CO_2} over In-doped TiO₂ catalyst is 60 bar⁻¹, slightly higher than the adsorption equilibrium constant of H₂O ($K_{H_2O} = 50$ bar⁻¹). These results reveal effective adsorption of CO₂ and H₂O vapors over the larger mesoporous In-doped TiO₂ catalyst surface area. The reaction rate constant for CO production is 3.2 times lower than for CH₄. Thus, the production of CO is more efficient than CH₄ at lower activation energy as discussed in the reaction mechanism when initially CO is produced, and then later converted to CH₄.

4. Conclusions

Indium (In) doped TiO₂ nanoparticles were synthesized by sol–gel single step method for photocatalytic CO₂ reduction with H₂O vapors in a cell type photoreactor. By doping TiO₂ with In, pure anatase phase of TiO₂ was produced with smaller particle size, larger surface area and mesoporous structure. UV–vis results revealed red shift in TiO₂ band gap, while the band for In-doped TiO₂ samples was slightly enlarged. The presence of In-metal in TiO₂ also increased active surface area and suppressed recombination of photogenerated electron–hole (e⁻/h⁺) pairs. XPS analysis showed that In was distributed over TiO₂ in metal state. Yield rates of CH₄ and CO as the main products over 10 wt.% In-doped TiO₂ catalyst were 243.75 and 81.25 μmole g-catal.⁻¹ h⁻¹, respectively under UV-light irradiation at 0.20 bars reactor pressure, 373 K reaction temperature and CO₂/H₂O feed ratio 1.43. The other products in significant amount were C₂H₄ and C₂H₆ with traces of C₃H₆ and C₃H₈. The selectivity of CH₄ production over TiO₂ was 40%, and increased to 70% over In-doped TiO₂ nanoparticles. The yields of CH₄ and CO over In-doped TiO₂ catalysts were 7.9 and 2-folds higher than TiO₂, respectively. The higher yield rates over In-doped TiO₂ catalyst were possibly due to higher active surface area, efficient production and inhibited recombination of electron–hole (e⁻/h⁺) pairs. The plausible pathways and reaction mechanisms were also suggested. Langmuir–Hinshelwood model fitted well with experimental data.

Acknowledgements

The authors would like to extend their deepest appreciation to the Ministry of Higher Education (MOHE) and Universiti Teknologi Malaysia for financial support of this research under LRGS (Long-term Research Grant Scheme) (Vot 4L800), RUG (Research University Grant) (Vot 00H49) and FRGS (Fundamental Research Grant Scheme) (Vot 4F404). The authors are also thankful to School of Engineering, Monash University Sunway campus for UV–vis spectrophotometer characterization.

References

- [1] M. Tahir, N.S. Amin, *Renew. Sustain. Energy Rev.* 25 (2013) 560–579.
- [2] G. Qin, Y. Zhang, X. Ke, X. Tong, Z. Sun, M. Liang, S. Xue, *Appl. Catal. B: Environ.* 129 (2013) 599–605.
- [3] T. Inoue, F. Akira, K. Satoshi, H. Kenichi, *Nature* 277 (1979) 637–638.
- [4] H. Yamashita, A. Shiga, S.-i. Kawasaki, Y. Ichihashi, S. Ehara, M. Anpo, *Energy Convers. Manage.* 36 (1995) 617–620.
- [5] K. Mori, H. Yamashita, M. Anpo, *RSC Adv.* 2 (2012) 3165–3172.
- [6] K. Ikeue, H. Yamashita, M. Anpo, T. Takewaki, *J. Phys. Chem. B* 105 (2001) 8350–8355.
- [7] M. Anpo, H. Yamashita, K. Ikeue, Y. Fujii, S.G. Zhang, Y. Ichihashi, D.R. Park, Y. Suzuki, K. Koyano, T. Tatsumi, *Catal. Today* 44 (1998) 327–332.
- [8] M. Tahir, N.S. Amin, *Energy Convers. Manage.* 76 (2013) 194–214.
- [9] T.T. Le, M.S. Akhtar, D.M. Park, J.C. Lee, O.B. Yang, *Appl. Catal. B: Environ.* 111 (2012) 397–401.
- [10] P.L. Richardson, M.L.N. Perdigoto, W. Wang, R.J.G. Lopes, *Appl. Catal. B: Environ.* 126 (2012) 200–207.
- [11] Y. Li, W.N. Wang, Z.L. Zhan, M.H. Woo, C.Y. Wu, P. Biswas, *Appl. Catal. B: Environ.* 100 (2010) 386–392.
- [12] L.J. Liu, F. Gao, H.L. Zhao, Y. Li, *Appl. Catal. B: Environ.* 134 (2013) 349–358.
- [13] O. Ola, M. Maroto-Valer, D. Liu, S. Mackintosh, C.-W. Lee, J.C.S. Wu, *Appl. Catal. B: Environ.* 126 (2012) 172–179.
- [14] X.K. Li, Z.J. Zhuang, W. Li, H.Q. Pan, *Appl. Catal. A: Gen.* 429 (2012) 31–38.
- [15] Q.Y. Zhang, Y. Li, E.A. Ackerman, M. Gajdardziska-Josifovska, H.L. Li, *Appl. Catal. A: Gen.* 400 (2011) 195–202.
- [16] O.K. Varghese, M. Paulose, T.J. Latempa, C.A. Grimes, *Nano Lett.* 9 (2009) 731–737.
- [17] K. Kočí, K. Zatloukalová, L. Obalová, S. Krejčíková, Z. Lacný, L. Čapek, A. Hospodková, O. Šolcová, *Chin. J. Catal.* 32 (2011) 812–815.
- [18] M. Tahir, N.S. Amin, *Appl. Catal. A: Gen.* 467 (2013) 483–496.
- [19] Yanlong Yu, Enjun Wang, Jixiang Yuan, Y. Cao, *Appl. Surf. Sci.* 273 (2013) 638–644.
- [20] E.J. Wang, W.S. Yang, Y.A. Cao, *J. Phys. Chem. C* 113 (2009) 20912–20917.

- [21] Tomoaki Houzouji, Nobuhiro Saito, Akihiko Kudo, T. Sakata, *Chem. Phys. Lett.* 254 (1996) 109–113.
- [22] Huihu Wang, J.L. Fariab, Shijie Donga, Y. Chang, *Mater. Sci. Eng. B* 177 (2012) 913–919.
- [23] M. Tahir, N.S. Amin, *Appl. Catal. B: Environ.* 142 (2013) 512–522.
- [24] M. Hinojosa-Reyes, S. Arriaga, L.A. Díaz-Torres, V. Rodríguez-González, *Chem. Eng. J.* 224 (2013) 106–113.
- [25] S.K. Poznyak, D.V. Talapin, A.I. Kulak, *J. Phys. Chem. B* 105 (2001) 4816–4823.
- [26] K.R. Reyes-Gil, E.A. Reyes-García, D. Raftery, *J. Phys. Chem. C* (2007) 14579–14588.
- [27] V. Rodríguez-González, R. Gómez, M. Moscota-Santillan, J. Amouroux, *J. Sol-Gel Sci. Technol.* 42 (2007) 165–171.
- [28] Xia Yang, Yonghui Wang, Leilei Xu, Xiaodan Yu, Y. Guo, *J. Phys. Chem. C* 112 (2008) 11481–11489.
- [29] S. Nakagawa, A. Kudo, M. Azuma, T. Sakata, *J. Electroanal. Chem.* 308 (1991) 339–343.
- [30] A.A. Ismail, D.W. Bahnemann, S.A. Al-Sayari, *Appl. Catal. A: Gen.* 431 (2012) 62–68.
- [31] J.C.S. Wu, H.-M. Lin, C.-L. Lai, *Appl. Catal. A: Gen.* 296 (2005) 194–200.
- [32] F. Saladin, I. Alxneit, *J. Chem. Soc. Farad. Trans.* 93 (1997) 4159–4163.
- [33] P.-Y. Liou, S.-C. Chen, J.C.S. Wu, D. Liu, S. Mackintosh, M. Maroto-Valer, R. Linforth, *Energy Environ. Sci.* 4 (2011) 1487.
- [34] M. Tahir, N.S. Amin, *Chem. Eng. J.* 230 (2013) 314–327.
- [35] S.S. Tan, L. Zou, E. Hu, *Catal. Today* 115 (2006) 269–273.
- [36] S.S. Tan, L. Zou, E. Hu, *Catal. Today* 131 (2008) 125–129.
- [37] K. Koci, L. Obalova, O. Solcova, *Chem. Process. Eng. – Inz.* 31 (2010) 395–407.